

# Automated Camera Stabilization and Calibration for Intelligent Transportation Systems

Marcel Bruckner  
Technische Universität München  
Boltzmannstraße 15, 85748 Garching  
[marcel.bruckner@tum.de](mailto:marcel.bruckner@tum.de)

## Abstract

*In the emerging field of Intelligent Transportation Systems one main challenge is the fusion of different sensor types. To fuse the measurements exactly each sensor needs to be free from noise and calibrated accurately. In this work we focus on two problems resulting from environmental influences on RGB cameras within the Providentia++ project.*

*First we propose an online vision-based pipeline to remove motion jitter from camera streams to dynamically stabilize the video feed. We show that our approach based on visual features and an image space homographic transformation significantly stabilizes the frames regarding the optical flow as measure. By exemplary tracking objects and measuring their travelled pixel distance we show a substantial decrease of the jittery image motion.*

*Second we propose an online Bundle Adjustment formulation based on the reprojection-error to statically calibrate separate RGB-only cameras w.r.t. a high definition map and to mitigate drift of the intrinsic and extrinsic camera parameters over time. By relaxing the minimization problem using a 1D-approximation of road signs we achieve high accuracy in the calibration of the cameras. We derive the minimal number of correspondences needed between the video stream and the map, the structure they have to exceed and give lower bounds on the remaining calibration errors.*

**Keywords**— Intelligent Transportation Systems, Computer Vision, Video Stabilization, Feature Detection, Feature Matching, Camera Calibration, Bundle Adjustment, Reprojection-Error, Optimization, OpenDRIVE

## 1. Introduction

Within the *Providentia++* project [14], a section of the highway A9 between Munich and Nuremberg was converted to a testing site for autonomous driving. As part of this, a large sensor network system has been set up along the highway to allow monitoring and steering of traffic as well as to improve the coordination between autonomous and traditional cars. The primary task of the

intelligent transportation system (ITS) is to create a digital traffic twin that accurately represents the physical road situation in real-time. Based on this digital twin, the smart infrastructure can provide a far-reaching and comprehensive view to the drivers and autonomous vehicles in order to improve their situational awareness within the current traffic environment.

A key challenge of ITS lies in the reliable and accurate calibration of the different sensors. The calibration is especially challenging when the sensor is subject to real-life disturbances like vibration of its mounting pole caused by wind or displacements due to temperature expansion. In this work we focus on removing the noise introduced by these disturbances and its implications for the vision system built upon cameras mounted to gantry bridges.

We propose two computer vision-based approaches to tackle the environmental influences and to remove noise from the system. The solved problems can be roughly grouped into problems concerning the dynamic stabilization of the video feed and the static calibration of the camera setup.

**Dynamic Stabilization** The cameras are constantly exposed to wind and vibrations from passing vehicles. These influences propagate into the video stream and result in jittery motion of the images. We propose a pipeline to counteract the shaky motions of the cameras using a digital image stabilization approach. The approach is based on visual image features that are matched between the current and a stable reference frame. The feature matching is used to minimize the reprojection-error between the frames and results in a homographic transformation. We use the transformation to align the static backgrounds of the frames, thus mitigating the real-world motion of the camera in image space.

**Static Calibration** We track and predict the real-world location of the vehicles in the test area to pass this information to the drivers and autonomous vehicles. To accurately predict the locations the system needs to be calibrated precisely towards a global reference frame. This is a time consuming process that often has to be done by hand. The cameras translational, rotational and intrinsic parameters decalibrate over time due to environmental influences on the mounting constructions and gantry bridges as well as from the natural wear of the materials.

Within the project high definition maps (HD maps) of the enclosed environment are used extensively. These HD maps offer

approximations of the real-world positions of the highway lanes, the gantry bridges, objects like poles and permanent delineators and traffic signals like speed limits or exit markers. We use this spatial information and a mapping from the objects to pixels in the video frame to solve a Bundle Adjustment (BA) problem by minimizing the reprojection-error. We jointly optimize for the cameras intrinsic and extrinsic parameters as well as the real-world locations to recover the camera poses from the observations.

**Code Repositories** The code for the dynamic stabilization, static calibration and object position retrieval from the HD maps are accessible via two GitHub repositories: <https://github.com/Brucknem/GuidedResearch> and <https://github.com/Brucknem/OpenDRIVE>.

## 2. Related Work

There are many ITS projects emerging recently [13, 4, 5, 1]. They propose novel approaches to the detection, tracking and traffic prediction problems that arise with the goal to provide additional environment information to human drivers and autonomous vehicles. Erdelean *et al.* [8] give a detailed overview over the existing projects up to the year 2019.

In the *Test Area Autonomous Driving Baden-Württemberg* [11] (TAADBW) project multiple optical camera sensors are attached to large poles with overlapping fields of view. They calibrate their cameras relative to a high-precision map and assume the calibration and the intrinsic camera parameters to be static during runtime. The team relies on a manual a-priori selection of visual landmarks and perform calibration at system startup. The team of the TAADBW estimate the extrinsic calibration with exact world position from the map by minimizing the squared distances between the visible landmarks and the respective projected objects. The large overlaps in the fields of view in their setup allow a global optimization strategy. This is not feasible in our project due to the small overlaps in the fields of view between the cameras [14] and associating pixels within the multi-view setup is an inherently hard problem.

Müller *et al.* [19] present an approach based on a cooperative intelligent vehicle. The vehicle moves through the scene and passes cooperative awareness messages containing positional information from the vehicle to the infrastructure. This removes the need for overlapping fields of view completely and enables a fully automated and sensor-independent registration. The team calibrates a multitude of different sensor types to the world frame and recovers their extrinsic parameters.

Calibration between cameras and radar sensors has been solved previously by Schöller *et al.* within the *Providentia++* project [14].

An overview over the general structure of Bundle Adjustment problems as used in Section 3.2 is given by Triggs *et al.* in [23].

## 3. Approach

In this paper we propose two algorithms to solve distinct problems that arise from real-world disturbances that act upon the ITS.

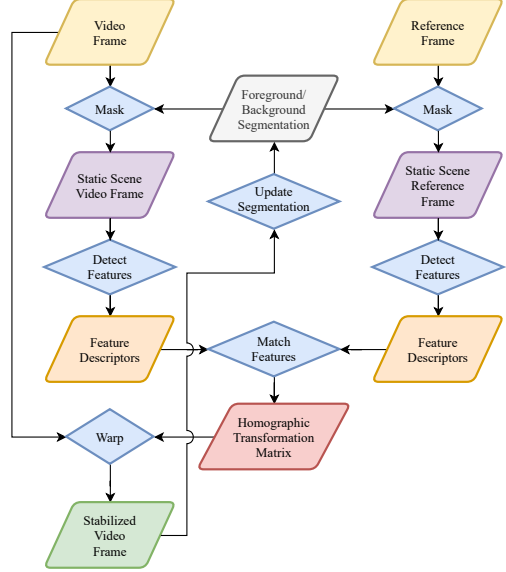


Figure 1. The proposed dynamic stabilization pipeline. The input is the video and a stable reference frame. The frames are segmented into the foreground and background to extract the static scene. On the static scene visual features are detected and the feature descriptors are matched. We use the homographic transformation minimizing the reprojection-error based on the matching to warp the video frame. The stabilized frame is used to update the background segmentation mask.

### 3.1. Dynamic Stabilization

The camera sensors used in the project are mounted to gantry bridges spanning over the highway. Environmental influences, *e.g.* wind or vibrations from passing vehicles, bring the bridges into a swinging state that spreads onto the cameras. This unwanted real world movement propagates into the video feeds output by the cameras and introduces jittery motion in image space. We assume the cameras to be mostly static, thus we only face disturbances within a small range around the resting position. Nonetheless, the small disturbances get amplified by the huge distances covered by the cameras and introduce substantial error.

To mitigate the noise added by the jittery motion we propose the pipeline displayed in Figure 1 and explained in the following.

**Extract Static Background** We stabilize the input frame by minimizing the reprojection-error between the video frame and the reference frame, thus aligning the images. This alignment is based on the matching of features between the frames, whereas we do not align the moving vehicles, but only the static non-moving background, *e.g.* the road, poles, guardrails and bridges. We assume that the background does not move in the real world, thus aligning it during image warping ensures that the scene stays static and only the vehicles real movement is kept. Hence, we extract the static background from the input frame and the stable reference frame using a background segmentation based on the *Improved Adaptive Gaussian Mixture Model for Background Subtraction* proposed by Zoran Zivkovic *et al.* [24, 25, 7].



Figure 2. Left: The input frame. Right: The stable reference frame. The colorful lines display the matching between image features. The ends of the lines are the location of the features.

**Feature Detection** We search the static background for pixel locations that are prominent and depict specific patterns that are unique and can easily be compared. The detected features describe the location based on different metrics, *e.g.* the local image gradient, oriented histograms or haar-like features [22]. Kumar *et al.* [15] give in depth descriptions of a multitude of feature detectors and descriptors.

We implemented the SURF [6] and ORB [21] feature detectors and descriptors and the Fast [12] feature detector with FREAK [2] feature descriptors. The algorithmic implementation is included in the OpenCV library [7].

**Feature Matching** We compare the detected features from the input frame with the features from the stable reference frame. A match is reported if the feature descriptors of two compared features surpass the Lowe’s ratio test [17] regarding some feature dependent metric [15]. These feature matches establish a spatial relationship in pixel space between the two frames. Figure 2 displays an exemplary feature matching.

We estimate a homographic transformation  $H$  that maps the homogeneous pixel locations  $(x_i, y_i, 1)^T$  of the input frame to the matched pixel locations  $(x'_i, y'_i, 1)^T$  in the stable reference frame. We minimize the reprojection-error between the pixels so that for each match  $i$  it holds

$$z_i * (x'_i, y'_i, 1)^T \sim H * (x_i, y_i, 1)^T \quad (1)$$

where  $z_i$  is the homogeneous component used in the perspective division. We use a RANSAC [10] based estimation procedure to robustify the minimization against outliers.

The algorithmic implementation is included in the OpenCV library [7].

**Image Alignment** We use the found homographic transformation to warp the whole input frame, thus aligning the background of the frames. As the keyframe is stable and does not change over time the current video frame is also stabilized. The alignment minimizes the motion of the static background scene and leaves only the real expected movement of the vehicles.

**Update of Background Segmentation** We use the stabilized frame to update the segmentation of the foreground and background. We assume the motion between frames to be relatively small, thus we use the segmentation of the stabilized frame for

the next frame. This reduces the search space for the feature detectors and prohibits matches between static scene and dynamic foreground objects.

### 3.2. Static Calibration

ITS are inherently dependent on the calibration of the different sensors. The system has to know the poses of the different sensors relative to some reference coordinate system to accurately measure the position of vehicles within the single sensor ranges and at the overlapping boundaries.

We propose a calibration procedure based on a Bundle Adjustment (BA) problem formulation. We map visual landmarks in the video feed to their partially known world positions from high definition road maps (HD maps). We recover the pose by jointly optimizing for the camera intrinsic and extrinsic parameters as well as the real world positions of the landmarks.

**Retrieve Objects from High Definition Maps** In our project we use HD maps in the OpenDRIVE standard format. In this work we focus on the permanent delineator (PD) objects that are easily visible in the video feeds.

We extract the world position of the PDs using the mathematical operations defined in the OpenDRIVE standard. This gives us the base origin point  $o = (x, y, z)^T$  of the PDs in the Universal Transverse Mercator (UTM) projection [16, 20]. The point  $o$  is the real world position of the lower end of the PD where it touches the ground or another object. Additionally, we retrieve a directional heading axis  $d = (x, y, z)^T$  and the height  $h$  of the PD.

**1D Approximation of Objects** In the original BA setting the optimization is done jointly over multiple cameras and observations, and the arising stereo vision problem is solved jointly for the 3D positions of the objects and the camera parameters. For this system of equations to be solvable it requires multiple cameras from different viewing angles and large overlapping fields of view between the cameras.

In our project we have neither of the requirements and thus calibrate each camera separately to the HD map. We relax the BA problem by the 1D line approximation of the PDs

$$S = \{o + \lambda * d : \lambda \in [0, h]\} \quad (2)$$

where  $S$  is the set of points along its central axis between the base at  $\lambda = 0$  and its top at  $\lambda = h$ . This approximation allows for a joint optimization of their world positions and the camera intrinsic and extrinsic parameters.

Section 4.3.2 derives a minimal number of points for the resulting system of equations to be solvable.

**Mapping Objects to Pixels** We solve the BA problem by minimizing the reprojection-error over the PDs. We thus require a set  $C$  of correspondences that map world points  $s_c$  of the PDs to their respective pixel  $p_c$ . Figure 3 displays an exemplary mapping from a HD map to the video feed.

This mapping is currently done by human interaction and not fully automated. We implemented an annotation tool to mark and create a list of pixels that can easily be mapped to the list of objects.



Figure 3. Left: The current camera frame. Right: A part of the HD map. Light blue lines: An exemplary mapping  $s_c \mapsto p_c$  from objects (right) to their corresponding pixels (left).

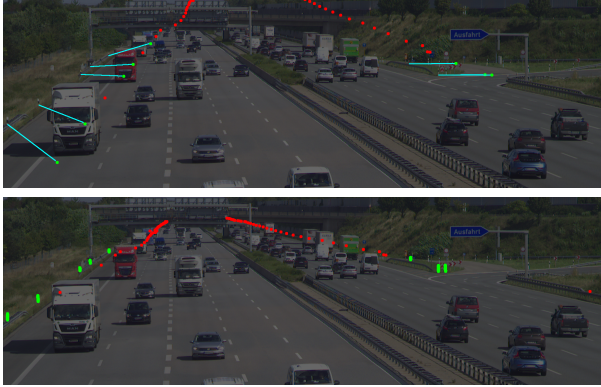


Figure 4. Top: Points of PDs mapped to pixel locations (green) and points without known corresponding pixels (red) rendered by a poorly calibrated camera model. The mapping from the projected points to their expected pixels is drawn in light blue. Bottom: The same points after the calibration procedure. The rendered positions of the mapped points align with their respective pixels. The drawn mapping disappears as the distances approach 0.

**Calibration Procedure** We model our cameras using the pin-hole camera model. The projection from points  $s_c = o_c + \lambda_c * h_c$  of the PDs world positions to pixels  $p_c$  is formulated as

$$p_c = \pi(R * T * (o_c + \lambda_c * h_c)) \quad (3)$$

where  $R$  is the cameras world rotation in Euler angles,  $T$  is the cameras world translation and  $\pi$  is the pinhole projection to image space based on the camera intrinsic parameters. The pinhole projection  $\pi$  is formulated as

$$z * \pi(x) = \begin{pmatrix} f_x, & 0, & c_x, & 0 \\ 0, & f_y, & c_y, & 0 \\ 0, & s, & 1, & 0 \end{pmatrix} * x \quad (4)$$

where  $x$  is an 3D input vector in homogeneous coordinates,  $f_x, f_y$  are the focal lengths in pixels,  $c_x, c_y$  is the principle point,  $s$  is the skew parameter and  $z$  is the homogeneous component used in the perspective division.

The optimal values for  $\pi, R, T$  are found if for all correspondences the distance between the expected pixel  $\hat{p}_c$  and the projected pixel  $p_c$  is minimal and it holds for all  $c$

$$0 = \hat{p}_c - \pi(R * T * (o_c + \lambda_c * h_c)) = \hat{p}_c - p_c \quad (5)$$

This places constraints on the values  $\pi, R, T$  can take and enables us to recover the camera pose, the intrinsic parameters and the 1D approximate positions relative to the  $\lambda$ s only from the correspondences.

Figure 4 displays rendering the PDs before and after calibration.

**Reprojection-Error Formulation** We solve the BA problem by minimizing a modified version of the least-squares reprojection-error  $E$  formulated as

$$\begin{aligned} E(P, S, \pi, T, R, W) = & \sum_{c \in C} \rho(\|w_c * [\hat{p}_c - p_c]\|_2^2) \\ & + \sum_{c \in C} \alpha * \rho(\|(1 - w_c)\|_2^2) \\ & + \sum_{c \in C} \beta * \rho(\|\Delta(\lambda_c, 0, h_c)\|_2^2) \\ & + \sum_{\pi_i \in \pi} \gamma * \rho(\|\Delta(\pi_i, \pi_i * 0.9, \pi_i * 1.1)\|_2^2) \\ & + \delta * \rho(\|\Delta(R_x, 60, 110)\|_2^2) \\ & + \delta * \rho(\|\Delta(R_y, -10, 10)\|_2^2) \end{aligned} \quad (6)$$

where  $P$  is the set of mapped pixels  $\hat{p}_c$  in the image and  $S$  is the set of mapped corresponding points  $s_c$  from the PDs. The additional weights  $w_c \in W$  are associated to the correspondences to downweight outliers and are enforced to stay near 1. We use a robust huber loss function  $\rho$  to further decrease the influence of outliers.

We guide the algorithm to feasible solutions by penalizing  $\lambda_c$  values that are negative or exceed the PDs height  $h_c$  using the distance

$$\Delta(x, l, u) = \begin{cases} x - u, & \text{if } x > u \\ x - l, & \text{if } x < l \\ 0, & \text{else} \end{cases} \quad (7)$$

from the interval  $[l, u]$ .

We rely on a rough initialization for the values  $\pi_i \in \pi$  and allow the optimizer to adjust the values within a  $\pm 0.1$  interval around the initialization.

Finally, we constrain the  $X$  axis rotation  $R_x$  (Pitch) to be within the interval  $[60, 110]$  degree and the  $Y$  axis rotation  $R_y$  (Roll) to be within the interval  $[-10, 10]$  degree, meaning that the camera has to be roughly in level and face horizontally.

The factors  $\alpha, \beta, \gamma, \delta$  are used to explicitly scale the remaining losses of the terms, thus giving them different influence on the optimizer. We saw empirically that good values for the factors are  $\alpha = 1 * 10^{100}, \beta = 2, \gamma = 10, \delta = 50$ .

**Initialization** In contrast to most BA problems our approach drops the need for good initialization. The regularization of the  $\lambda$  values gives the optimizer enough flexibility to optimize over the infinite space of possible values, but enforces the values of the  $\lambda$  to lie within the interval of  $\lambda \in [0, h]$ .

The optimizer calculates its own initial guess

$$T_0 = T(\bar{s}_x, \bar{s}_y, \bar{s}_z + \bar{d}) \quad (8)$$



Figure 5. The schematic camera setup along the highway A9. The cameras S40 Far and S40 Near are facing north, the cameras S50 Far and S50 Near are facing south.

for the camera translation based on the mean

$$\bar{s} = \frac{1}{|C|} \sum_{c \in C} o_c \quad (9)$$

of the base origin points  $o_c$  of the PDs and some distance  $\bar{d}$  from the mean.

The optimizer initializes the rotation

$$R_0 = R(x, y, z) \quad (10)$$

based on  $x, y, z$  Euler angle values drawn from the uniform distribution  $U(-35, 35)$ , where  $R(0, 0, 0)$  is the camera facing in negative Z direction onto the mean  $\bar{s}$ . This initialization ensures that all points lie in front of the camera and can be projected onto the image plane.

It is sufficient to initialize  $\lambda_c = 0$  for all correspondences.

## 4. Evaluation

We assure the correctness and quantify the improvements resulting from the algorithms by an empirical study on the video streams of the highway cameras.

### 4.1. Study Objects

We use video recordings from the four cameras mounted to the two gantry bridges internally named S40 and S50. The schematic camera setup is displayed in Figure 5.

The dataset consists of four recordings, each with a length of 1495 frames over  $\sim 60$  seconds at 25 frames per second. The recordings are taken on a day with strong winds to ensure high jitter in the video feed to optimally test the dynamic stabilization pipeline described in Section 3.1.

### 4.2. Dynamic Stabilization

We evaluate and compare three pipeline instances based on the SURF [6, 7] feature detector (SURF), ORB [21, 7] feature detector (ORB) and FAST [12, 7] feature detector with FREAK [2, 7] feature descriptors (FAST) and present two measures to evaluate the dynamic stabilization pipelines.

#### 4.2.1 Optical Flow

The optical flow is a 2D vector field where each vector is a displacement vector showing the movement of points between frames

caused by movement of the objects or cameras. It describes the apparent motion of image objects between two consecutive frames.

We use the dense optical flow estimation algorithm proposed by Farnebäck [9, 7] to measure the displacement of each pixel between the frames. We calculate the mean displacement over the whole frame to get a measure for the total motion in the image.

Figure 6 displays one frame of optical flow calculated pre and after stabilization. It qualitatively shows that the static background scene is dark in the stabilized frames which indicates a low optical flow and thus nearly no movement. We see a car driving, indicated by the yellow patch, that remains as expected using SURF and ORB, but gets filtered out by FAST. This problem is described in Section 4.2.1.

Figure 7 displays the mean pixel displacement (MPD) per frame calculated as the mean of the lengths of the vectors in the optical flow field and the damping as the difference of the MPD of the original and stabilized frames. It shows that the original frames have a MPD of up to 5 pixels per frame. This implies that on average every pixel on the dynamic scene and static background had moved by 5 pixels per frame. The displacement is damped by all of the stabilizers by a mean of up to 4.5 pixels, whereas the remaining displacement is due to the actually moving vehicles in the dynamic foreground.

Figure 8 displays the percentage of frames that are more stable than the original frame. We define a frame to be more stable if its MPD is lower than the MPD of the original frame. It shows that all for all stabilization pipeline instances more than 86.6% of frames are more stable, but SURF outperforms the other stabilizers with at least 95.6% of frames being more stable. Nonetheless, the remaining percentages of frames do not necessarily imply the frames to be worse as Section 4.2.1 states.

We included plots for the MPD and the damping for the other three cameras in the Appendix (Section 7).

**Problem of Optical Flow as a Measure** Optical flow cannot distinguish between dynamically moving objects and static scene. This is especially a problem when a jitter of the camera moves the pixels in the opposite direction as the vehicles path is pointing in image space. This jitter blurs the movement of the dynamic objects into the background and thus removes some of the real movement. The dynamic stabilization then reintroduces the real movement of the vehicle, thus showing some frames after stabilization to be worse than before.

This should be taken with caution as the optical flow cannot detect the relative motion and thus is not a definite measure for the jitter. Nonetheless, it hints at the overall stabilization capabilities of the presented pipeline, but cannot give a direct explanation for single worse frames.

#### 4.2.2 Path Length of Tracked Feature

We randomly took three sample vehicles per camera and tracked their pixel locations over the sequence. As the vehicles move through the image the bounding box of the object is found using the *Discriminative Correlation Filter With Channel and Spatial Reliability* proposed by Lukezic *et al.* [18, 7]. The center point of the bounding box is then written to disk and used as the predicted pixel location  $p$  of the vehicle.



Figure 6. From left to right: Original frame, stabilized using SURF, ORB and FAST. The dense optical flow displays the pixel displacement, the lighter the color the farther the displacement. The angle of displacement is color coded according to the HSV color circle. In the original frame the violet background color indicates a jittery camera movement. The car in the lower half is driving in the opposite direction as the camera jitters, indicated by the yellow patch.

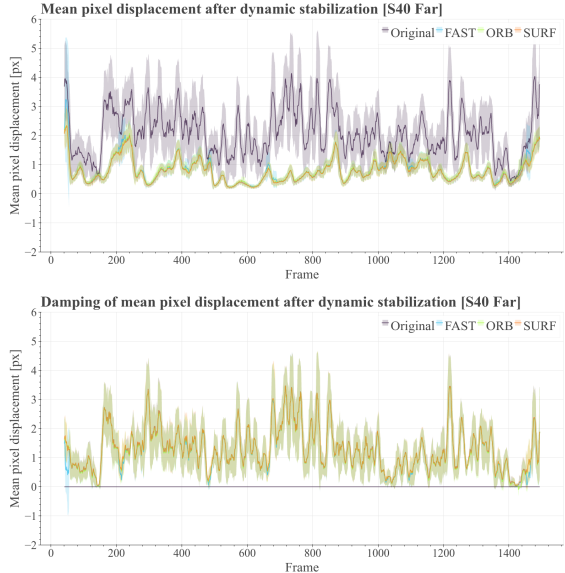


Figure 7. Top: Comparison of the three implemented dynamic stabilizers (SURF, ORB, FAST) and the original not stabilized video feed using optical flow as measure (lower is better). The graphs display the mean pixel shift at each frame. Bottom: The damping capabilities of the same three stabilizers (higher is better). The graphs approximate the removed jitter in the mean pixel shift between the original video and the stabilizer at each frame. For visualization the values are filtered using the rolling mean over 12 frames. The light areas display the standard deviation within the window.

We only track in the original frame to remove inaccuracies in the tracking and use the homographic transformation matrix from [Equation \(1\)](#) that stabilizes the frame to also stabilize the bounding boxes. This gives us comparable results for the pixel locations.

We calculate the travelled distance of the pixel locations of the objects as they move through the image. This distance is a direct measure for the jittery motion in the image as the motion introduces large jumps of the tracked positions, thus directly increasing the travelled distance.

The travelled distance is formulated as the arc length

$$arc(vehicle) = \sum_{n=1}^{|frames|} \|p_i - p_{i-1}\|_2 \quad (11)$$

based on the finite differences between consecutive tracked posi-

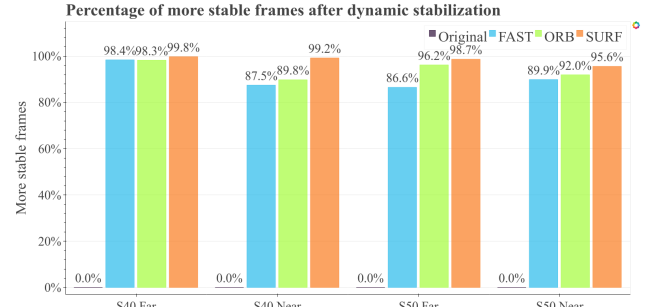


Figure 8. Comparison of the percentages of more stable frames after dynamic stabilization per camera and stabilizer. A processed frame is classified as more stable if the MPD is lower than for the original frame.

tions. To get comparable results a normalization

$$nar_{stabilizer}(vehicle) = \frac{arc_{stabilizer}(vehicle)}{arc_{original}(vehicle)} \quad (12)$$

is performed by the arc length of the original video frame.

[Figure 9](#) displays the vehicles tracked in the video sequence taken from the camera S40 Far. There is one red truck, a black pickup and a white car taken as random samples. The tracking is performed as long as the vehicles are visible. It shows that the travelled distances of the pixels after dynamic stabilization remain at between 43% and 68.4% compared to the original one. This implies that much of the additional motion introduced by the environmental influences is removed and the remaining path displays the real projected path of the vehicle.

We included plots for the tracked pixel locations and the comparison of the arc lengths for the other three cameras in the Appendix ([Section 7](#)).

#### 4.2.3 Speed Comparison

[Table 1](#) compares the average time needed to stabilize a frame per stabilizer instance. It shows that, although the name, the FAST stabilizer is the slowest, followed by SURF and beaten by ORB. Nonetheless, all stabilizers run at more than 50 frames per second and are thus all realtime capable.



Figure 9. Left: The exemplary vehicles tracked through the video sequence of the camera S40 Near and their bounding boxes. Right: The corresponding normalized arc lengths of the pixel path. The removed jitter is directly proportional to the decrease in the normalized arc lengths, as the tracked pixels only follow the real vehicles movements after stabilization.

| Stabilizer | Time [ms] | $\sigma$ [ms] |
|------------|-----------|---------------|
| FAST       | 18.649    | 2.102         |
| ORB        | 14.816    | 1.466         |
| SURF       | 16.058    | 1.443         |

Table 1. Comparison of the average milliseconds needed to stabilize the frame and the respective standard deviation in milliseconds per stabilizer instance.

### 4.3. Static calibration

In the following we evaluate the implemented static calibration algorithm and assess the possible algorithmic and systematic errors.

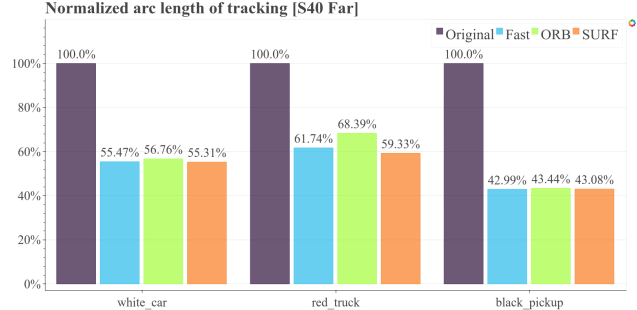
#### 4.3.1 Ensure Absence of Systematic Errors

We solve the BA problem proposed in [Section 3.2](#) by minimizing the reprojection-error as formulated in [Equation \(6\)](#). The algorithm converges to a pair of optimal translation  $T$  and rotation  $R$  values for the camera pose. These  $T, R$  values best describe the camera pose relative to the mapped objects as stated in [Equation \(3\)](#).

Using a maps provider we assured that the resulting values are within reasonable ranges and that there are no systematic errors in the optimization. [Figure 10](#) displays the positions of the four cameras and their respective looking directions. It shows that except for the camera S50 Far the expected position is within the expectable range around the actual position. All cameras are looking along the highway as expected. The far placement of camera S50 Far is due to inaccuracies in the mapping.

#### 4.3.2 Number of Correspondences Needed for Convergence

The correspondences build up a system of linear equations as described in [Equation \(3\)](#). This system of equations is solvable if the number of constraints on the parameters is equal to or exceeds the degrees of freedom in the system, thus being over constrained. This is the case if for the number  $|C|$  of correspondences it holds



that

$$\begin{aligned} 2 * |C| &\geq 5 + 3 + 3 + 1 * |C| \\ |C| &\geq 11 \end{aligned} \quad (13)$$

as each of the expected pixels  $\hat{p}_c$  gives us two constraints and we optimize for the 5 intrinsic parameters, 3 extrinsic translation parameters, 3 extrinsic rotation parameters and one  $\lambda_c$  parameter per correspondence. It shows that 11 points are enough to recover the pose, though more points improve the robustness of the algorithm.

#### 4.3.3 Structure of Correspondences

We empirically saw that recovering the camera pose performs best when there are at least two correspondences per object. These correspondences need to be the top and bottom most visible pixel of the object. If there exists only 1 or a low number of dense packed pixels the algorithm cannot precisely recover the camera pose as it is free to move the correspondences along the center line of the object. The algorithm therefore cannot distinguish solutions where it places the camera low, thus projecting a high point of an object to a low pixel correspondence, and solutions where it places the camera high and lowers the world position of the correspondence along the center line.

#### 4.3.4 Expectable Error Bounds

Due to measurement uncertainty in the camera sensors we expect some remaining error after pose estimation. We derive a lower bound on this error starting from the optimized focal length  $f_{px}$  in pixels, the sensor width  $w_{mm}$  in millimeters and  $w_{px}$  in pixels. We use the focal length in millimeters given by

$$f_{mm} = f_{px} * \frac{w_{mm}}{w_{px}} \quad (14)$$

to calculate the field of view (FOV) in radians by

$$FOV_x = 2 * \arctan \left( \frac{f_{mm}}{2 * w_{mm}} \right) \quad (15)$$

Equivalent for the  $FOV_y$  with the height of the sensor  $h_{mm}$ . The angle  $\alpha_{px}$  in radians spanned by each pixel is calculated by

$$\alpha_{px} = \frac{w_{px}}{FOV_x} \quad (16)$$

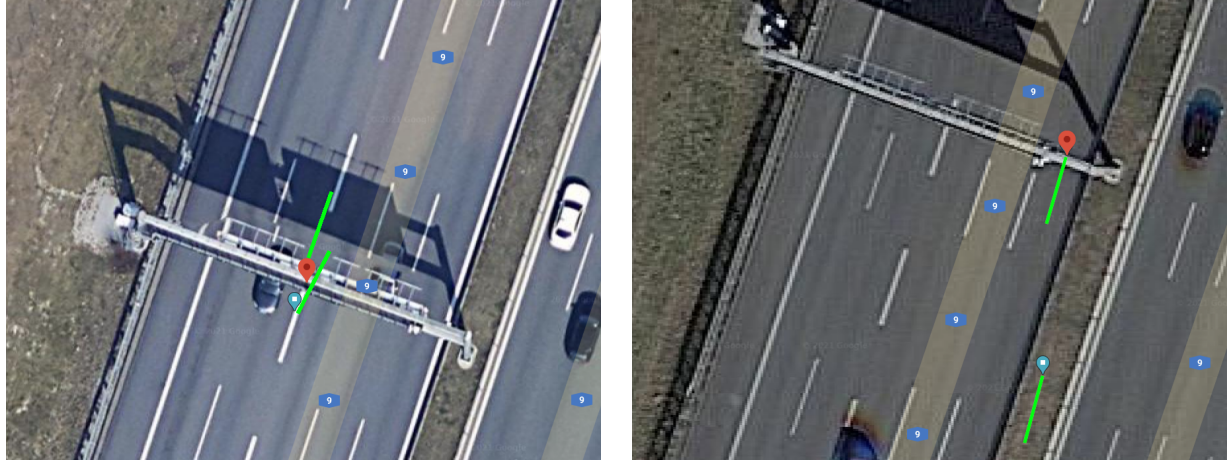


Figure 10. Left: The positions of the cameras S40 Near (red) and S40 Far (blue) and their respective looking directions (green). Right: The positions of the cameras S50 Near (red) and S50 Far (blue) and their respective looking directions (green). The rotations of the cameras are in a reasonable range so that the cameras look along the highway as expected. All cameras, except the S50 Far camera, are within reasonable translational bounds around their real world location as [Section 4.3.4](#) shows.

| Camera   | $f_{px}$ | $FOV_x[\circ]$ | $\alpha_{px}[rad]$ | $d[m]$ | $u[cm]$ |
|----------|----------|----------------|--------------------|--------|---------|
| S40 Far  | 8591     | 12.753         | $1.16e^{-4}$       | 200    | 2.32    |
| S40 Far  | 8591     | 12.753         | $1.16e^{-4}$       | 650    | 7.54    |
| S40 Near | 2735     | 38.678         | $3.52e^{-4}$       | 25     | 0.88    |
| S40 Near | 2735     | 38.678         | $3.52e^{-4}$       | 450    | 15.82   |
| S50 Far  | 8868     | 12.357         | $1.12e^{-4}$       | 200    | 2.22    |
| S50 Far  | 8868     | 12.357         | $1.12e^{-4}$       | 650    | 7.30    |
| S50 Near | 2747     | 38.527         | $3.50e^{-4}$       | 25     | 0.88    |
| S50 Near | 2747     | 38.527         | $3.50e^{-4}$       | 450    | 15.76   |

Table 2. The focal lengths  $f_{px}$ , fields of view  $FOV_x[\circ]$  and spanned angle per pixel  $\alpha_{px}[rad]$  compared to the measurement uncertainty  $u[cm]$  at some distance  $d[m]$  from the cameras. It shows a linear increase of the uncertainty proportional to the distance of the object from the camera.

Using trigonometry we can then calculate the uncertainty

$$u = \tan(\alpha_{px}) * d \quad (17)$$

of the camera as the spanned meters per pixel relative to the distance  $d$  from the camera.

[Table 2](#) displays the uncertainty for our cameras. It shows that the far cameras cannot distinguish between points that are  $\sim 2.2cm$  at the nearest visible distance from the camera ranging up to  $\sim 7.54cm$  at the farthest distance. The near cameras cannot distinguish between points that are  $\sim 0.88cm$  at the nearest visible distance from the camera ranging up to  $\sim 15.82cm$  at the farthest distance.

Additional to the sensor uncertainties we are facing uncertainties in the HD maps. The positions of the used PDs are only precise within  $1cm - 3cm$ . This data uncertainty adds up with the measurement uncertainty introduced by the cameras.

The highest possible achievable precision for the translational parameters of the camera is bound by the uncertainty in the measurements and HD maps, as a misplacement of the camera can

only be detected if it is farther than the uncertainty of the sensors and HD maps. Nonetheless, in practice the imprecision will sum up and the translation parameters will drift inevitable. This implies that objects in close distance to the camera are more reliable when estimating the translation.

The rotational parameters can be estimated more precisely, as small rotational deviations introduce large deviations in the objects projected pixels. The expectable precision for the rotation is thus bound by the angle  $\alpha_{px}$  spanned per pixel, as a deviation by one  $\alpha_{px}$  would project the objects onto the next pixel. This implies that the precision of the rotation is at least in the range of  $1.12 * 10^{-4}$  to  $3.52 * 10^{-4}$  radians.

#### 4.3.5 Estimation of Algorithmic Error Bounds

We solve the BA problem proposed in [Section 3.2](#) by minimizing the reprojection-error as formulated in [Equation \(6\)](#). The optimization jointly optimizes for the 5 intrinsic parameters, 3 extrinsic translation parameters, 3 extrinsic rotation parameters and one  $\lambda_c$  parameter per correspondence. Convergence is reached when the gradient of the optimized parameters is zero and the found solution is a minimum. The resulting high-dimensional problem contains a multitude of local minima, whereas each represents a configuration for the camera pose that well explains the dependency ([Equation \(3\)](#)) between pixels, world objects and the camera.

[Figure 11](#) displays the resulting parameters for the camera S40 Far recorded over 250 runs. We plot each of the parameters against the remaining loss of the correspondences and the  $\lambda_c$ . For visualization only the relative remaining losses are plotted, as the absolute values have no valuable meaning. The translation parameters are in meters and relative to the UTM projection [16]. The rotation parameters are in degrees of Euler angles. The focal length is given in pixels.

The plots show that the standard deviation  $\sigma_T$  of the translations does not exceed  $6 * 10^{-8}m = 60nm$ ,  $\sigma_R$  of the rotation is at most  $2 * 10^{-9}deg$  and  $\sigma_\pi$  of the focal length is at most  $1 * 10^{-6}$

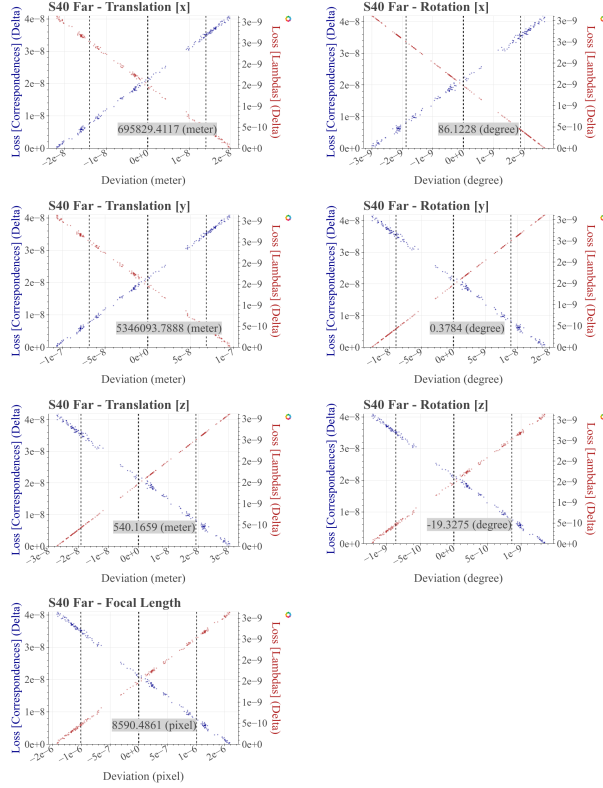


Figure 11. Left: The resulting translational parameters plotted against the remaining losses. Right: The resulting rotational parameters plotted against the remaining losses. Bottom: The resulting focal length plotted against the remaining losses. For visualization only the relative remaining losses are plotted, as the absolute values have no valuable meaning.

pixels. This implies that compared to the uncertainty introduced by the measurements (Section 4.3.4) the algorithmic error can be neglected.

We evaluate the algorithmic error for the remaining cameras in the Appendix (Section 7). The results are the same as expected and the distribution of the datapoints of the parameters and losses is dependent on the mapping and the viewed scene of the camera, thus the visible structures in the datapoints are arbitrary.

## 5. Future Work

The project leaves us with the opportunity to continue the research in multiple directions.

### 5.1. Varying Weather and Lighting Conditions

We tested and evaluated the implementations on recordings with good weather and lighting conditions, thus a next step is to test the implementations in bad weather and lighting conditions, *e.g.* by night, rain and snow. From our current perspective the feature based dynamic stabilization approach will suffer in performance as the homography estimation depend on features in the image space. By night and if the static background is occluded the stabilization pipeline will fail, although in these cases the complete

RGB image will be unusable at all.

We implemented the solver for the BA problem to include human interaction when mapping from PDs to pixels. The mapping will be harder in bad weather and lighting conditions based on the worse visibility of the landmarks. We propose an automatic mapping scheme in Section 5.3.2. This scheme will be affected by changing weather and lighting conditions as the detection of new landmarks is also based on the visibility of landmarks.

## 5.2. Dynamic Stabilization

We present two major improvements that can be done to extend the presented dynamic stabilization approach.

### 5.2.1 Warp Field Stabilization Based on Optical Flow

We use the optical flow to measure the performance of the stabilizers as described in Section 4.2.1. The optical flow is a 2D vector field where each vector is a displacement vector showing the movement of pixels between frames caused by movement of the objects or cameras. The image can be stabilized using the inverse vector field that also minimizes the reprojection error between frames.

### 5.2.2 Deep Learning Based Dynamic Stabilization

Based on the ongoing success of deep learning approaches in computer vision, especially of convolutional neural networks (CNN), a self-learning stabilization procedure might be developed. The CNN expects the current input and reference frame and outputs the homographic transformation or the warped frame. This might speed up the pipeline and inherently adds a measure for the uncertainty of the results by modelling the probability of the homographic transformation. This approach can be used to fuse the feature detection, matching and warping steps into one joint step that is learned by the CNN from labeled data.

## 5.3. Static Calibration

We present two major improvements that can be done to extend the presented static calibration approach.

### 5.3.1 Robustness Against Outliers

BA problems are inherently prone to outliers, as they greatly impact the shape of the reprojection-error loss landscape. To use the presented system in practice a RANSAC [10] or similar sample consensus based approach needs to be implemented. By evaluating the calibration multiple times with different subsets of correspondences a stable sample consensus can be found in asymptotically all runs. This will greatly impact the robustness of the calibration procedure against outliers, as they can be filtered out automatically by the algorithm.

### 5.3.2 Fully Automatic Static Calibration

We establish the mapping of the correspondences by hand, thus a human has to look up the ids of the landmarks in the HD maps

and assign them to their respective pixels. After an initial calibration that requires human interaction, an image region based approach might be used to automate this mapping. One can project the known base origin points of the objects from the HD maps into the current frame. Starting from the projected pixel locations one could search in a defined enclosing region to find pixels that clearly correspond to the objects by applying template, color or gradient matching approaches. The automatic detection of landmarks enables the system to perform fully automatic static self calibration.

### 5.3.3 Machine Learning Based Bundle Adjustment

Aravkin *et al.* [3] have shown that the BA problem can be modelled on top of a Student's-t distribution. The resulting statistical machine learning approach for the BA can be used to jointly estimate the camera parameters and world positions of objects, while at the same time being robust against outliers.

### 5.3.4 New High Definition Map

The newer OpenDRIVE standard also provides the possibility to include lane markings. These lane markings are easily detectable and can be used for the calibration procedure in conjunction with the object landmarks. This would greatly simplify the automatic detection and mapping procedures as described in [Section 5.3.2](#) as they are spatially more extend and thus easier to detect. Furthermore, the lane markings are always white or yellow which simplifies the detection. As shown in [Section 4.3.4](#) the static calibration is more precise the closer the correspondences are to the cameras. As there exists far more lane markings than objects, and with the markings being evenly distributed over the road the static calibration would benefit from this additional information.

## 6. Conclusion

In this paper we proposed two main improvements on the vision-based tracking system used in the *Providentia++* project [14].

We first presented a pipeline to dynamically stabilize jittery motion in the video streams of RGB cameras mounted to gantry bridges along a highway. We applied a homographic transformation in image space based on the matching of visual features between the current and a stable reference frame. We have shown that the stabilization substantially (up to 99.8%) improves the stability of the frames regarding the remaining mean pixel displacement. By tracking vehicles through the video sequence we have shown that the remaining length of the pixels path after stabilization is lowered by up to 57% compared to the not stabilized one and thus the jittery motion of the camera is compensated significantly after stabilization. Finally, we have shown that the dynamic stabilization pipeline is realtime capable with at least 50 processed frames per second.

We secondly presented the formulation of a single camera RGB-only Bundle Adjustment problem that is minimized using the reprojection-error to statically calibrate the camera setup to the reference system. We recover the cameras pose by jointly optimizing for the cameras intrinsic and extrinsic parameters as well as the real world position of viewed correspondences to a high definition map. We checked our results for the absence of systematic errors,

gave a lower bound on the number of correspondences needed for convergence and the structure the correspondences have to exceed. We evaluated the expectable error after pose estimation that arises from measurement uncertainties and imprecisions in the HD map and have shown that the deviations among the minima found by the optimization strategy are neglectable.

## References

- [1] Motilal Agrawal, Kurt Konolige, and Morten Rufus Blas. Censure: Center surround extrema for realtime feature detection and matching. In *European Conference on Computer Vision*, pages 102–115. Springer, 2008. [2](#)
- [2] A. Alahi, R. Ortiz, and P. Vandergheynst. Freak: Fast retina keypoint. In *2012 IEEE Conference on Computer Vision and Pattern Recognition*, pages 510–517, 2012. [3, 5](#)
- [3] Aleksandr Aravkin, Michael Styler, Zachary Moratto, Ara Nefian, and Michael Broxton. Student’s t robust bundle adjustment algorithm. *Proceedings / ICIP ... International Conference on Image Processing*, 11 2011. [10](#)
- [4] Eduardo Arnold, Mehrdad Dianati, Robert de Temple, and Saber Fallah. Cooperative perception for 3d object detection in driving scenarios using infrastructure sensors. *IEEE Transactions on Intelligent Transportation Systems*, 2020. [2](#)
- [5] E. Arnold, M. Dianati, R. de Temple, and S. Fallah. Cooperative perception for 3d object detection in driving scenarios using infrastructure sensors. *IEEE Transactions on Intelligent Transportation Systems*, pages 1–13, 2020. [2](#)
- [6] Herbert Bay, Tinne Tuytelaars, and Luc Van Gool. Surf: Speeded up robust features. In Aleš Leonardis, Horst Bischof, and Axel Pinz, editors, *Computer Vision – ECCV 2006*, pages 404–417, Berlin, Heidelberg, 2006. Springer Berlin Heidelberg. [3, 5](#)
- [7] G. Bradski. The OpenCV Library. *Dr. Dobb's Journal of Software Tools*, 2000. [2, 3, 5](#)
- [8] Isabela Erdelean, Abdelmename Hedhli, Martin Lamb, Niklas Strand, and Ewa Zofka. Catalogue of connected and automated driving test sites: Deliverable no2. 1. 2019. [2](#)
- [9] Gunnar Farnebäck. Two-frame motion estimation based on polynomial expansion. In Josef Bigun and Tomas Gustavsson, editors, *Image Analysis*, pages 363–370, Berlin, Heidelberg, 2003. Springer Berlin Heidelberg. [5](#)
- [10] Martin A Fischler and Robert C Bolles. Random sample consensus: a paradigm for model fitting with applications to image analysis and automated cartography. *Communications of the ACM*, 24(6):381–395, 1981. [3, 9](#)
- [11] Tobias Fleck, Karam Daaboul, Michael Weber, Philip Schörner, Marek Wehmer, Jens Doll, Stefan Orf, Nico Sußmann, Christian Hubschneider, Marc René Zofka, et al. Towards large scale urban traffic reference data: Smart infrastructure in the test area autonomous driving baden-württemberg. In *International Conference on Intelligent Autonomous Systems*, pages 964–982. Springer, 2018. [2](#)
- [12] Morteza Ghahremani, Yonghuai Liu, and Bernard Tiddeman. Ffd: Fast feature detector. *IEEE Transactions on Image Processing*, 30:1153–1168, 2021. [3, 5](#)
- [13] Frank Köster and Mathias Höhne. Testfeld für autonomes und vernetztes fahren in niedersachsen. 2017. [2](#)
- [14] Annkathrin Krämmer, Christoph Schöller, Dhiraj Gulati, Venkatnarayanan Lakshminarasimhan, Franz Kurz, Dominik Rosenbaum, Claus Lenz, and Alois Knoll. Providentia - a large-scale sensor system for the assistance of autonomous vehicles and its evaluation, 2020. [1, 2, 10](#)
- [15] Rekhil M Kumar and K Sreekumar. A survey on image feature descriptors. *Int J Comput Sci Inf Technol*, 5:7668–7673, 2014. [3](#)
- [16] Richard B Langley. The utm grid system. *GPS world*, 9(2):46–50, 1998. [3, 8](#)
- [17] David G. Lowe. Distinctive image features from scale-invariant keypoints. *Int. J. Comput. Vision*, 60(2):91–110, Nov. 2004. [3](#)
- [18] Alan Lukezic, Tomas Vojir, Luka Cehovin Zajc, Jiri Matas, and Matej Kristan. Discriminative correlation filter with channel and spatial reliability. In *Proceedings of the IEEE Conference on Computer Vision and Pattern Recognition (CVPR)*, July 2017. [5](#)
- [19] J. Müller, M. Herrmann, J. Strohbeck, V. Belagiannis, and M. Buchholz. Laci: Low-effort automatic calibration of infrastructure sensors. In *2019 IEEE Intelligent Transportation Systems Conference (ITSC)*, pages 3928–3933, 2019. [2](#)
- [20] PROJ contributors. *PROJ coordinate transformation software library*. Open Source Geospatial Foundation, 2021. [3](#)
- [21] E. Rublee, V. Rabaud, K. Konolige, and G. Bradski. Orb: An efficient alternative to sift or surf. In *2011 International Conference on Computer Vision*, pages 2564–2571, Nov 2011. [3, 5](#)
- [22] David G Stork, Richard O Duda, Peter E Hart, and D Stork. Pattern classification. *A Wiley-Interscience Publication*, 2001. [3](#)
- [23] Bill Triggs, Philip F. McLauchlan, Richard I. Hartley, and Andrew W. Fitzgibbon. Bundle adjustment — a modern synthesis. In Bill Triggs, Andrew Zisserman, and Richard Szeliski, editors, *Vision Algorithms: Theory and Practice*, pages 298–372, Berlin, Heidelberg, 2000. Springer Berlin Heidelberg. [2](#)
- [24] Zoran Zivkovic. Improved adaptive gaussian mixture model for background subtraction. In *Proceedings of the Pattern Recognition, 17th International Conference on (ICPR'04) Volume 2 - Volume 02*, ICPR '04, page 28–31, USA, 2004. IEEE Computer Society. [2](#)
- [25] Zoran Zivkovic and Ferdinand van der Heijden. Efficient adaptive density estimation per image pixel for the task of background subtraction. *Pattern Recogn. Lett.*, 27(7):773–780, May 2006. [2](#)

## **7. Appendix**

To declutter the report we moved many of the plots in this section. Please see the next pages for the plots.

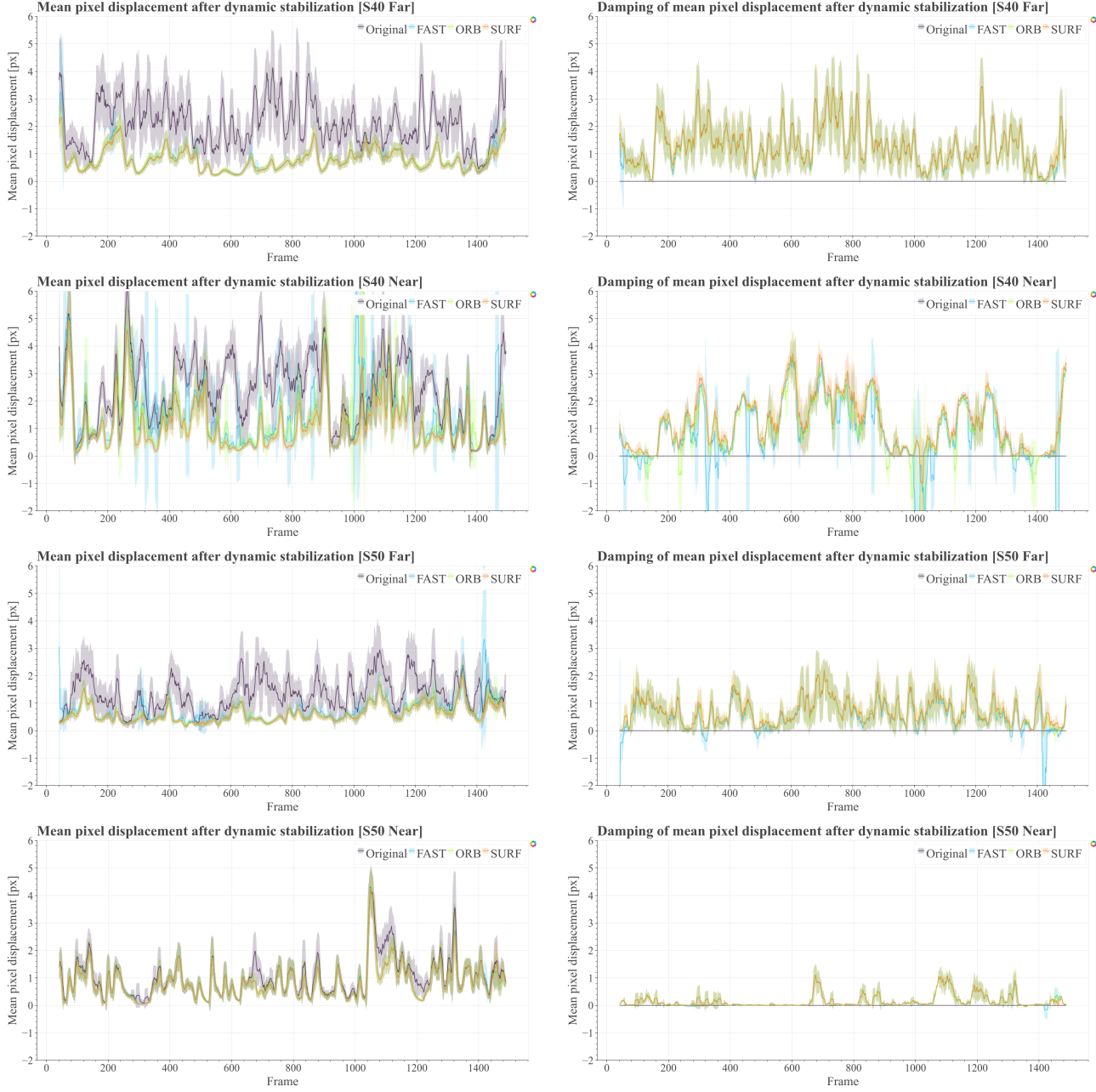


Figure 12. Top to bottom: The mean pixel displacements recorded for the four cameras used in the setup. Left: The mean pixel shifts after stabilization with SURF, ORB and FAST compared to the original not stabilized video feed using optical flow as measure (lower is better). Right: The damping of the mean pixel shifts of the same three stabilizers (higher is better). The graphs approximate the removed jitter in the mean pixel shift between the original video and the stabilizers at each frame.  
 For visualization the values are filtered using the rolling mean over 12 frames. The light areas display the standard deviation within the window.  
 It shows that for each of the stabilizers the damping is substantial, removes most of the jitter introduced by environmental influences and leaves only wanted movement of vehicles in the dynamic foreground.

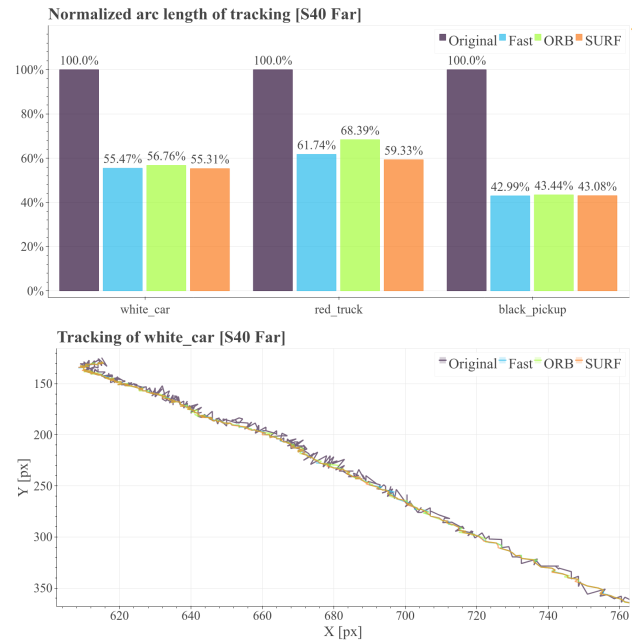
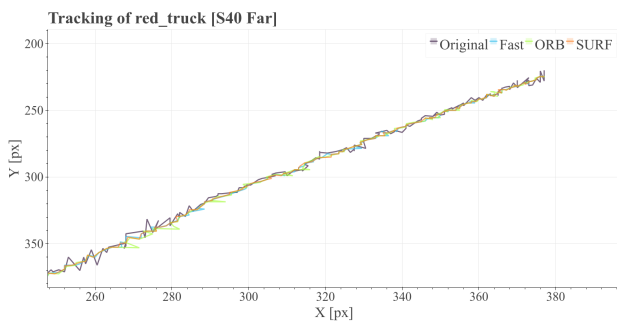
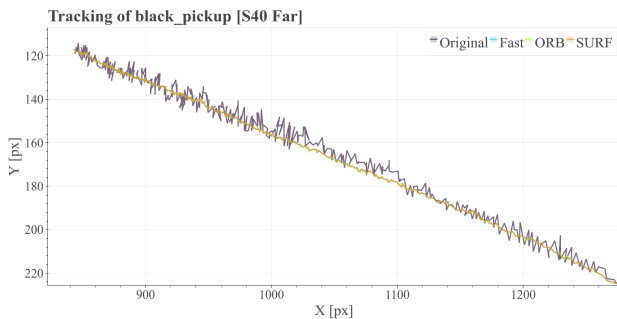


Figure 13. Top left: The tracked vehicles in the camera S40 Far marked by their bounding boxes. Top right: The normalized arc lengths representing the path of the tracked pixels through the image. Bottom graphs: The tracked pixel locations of the vehicles as they move through the scene for the original video feed and the stabilized ones. The jittery motion of the camera can be clearly seen by the chaotic movement of the pixels in the original sequence. After stabilization the pixels move much more smoothly through the images, whereas the remaining jitter is mostly due to inaccuracies in the tracking.

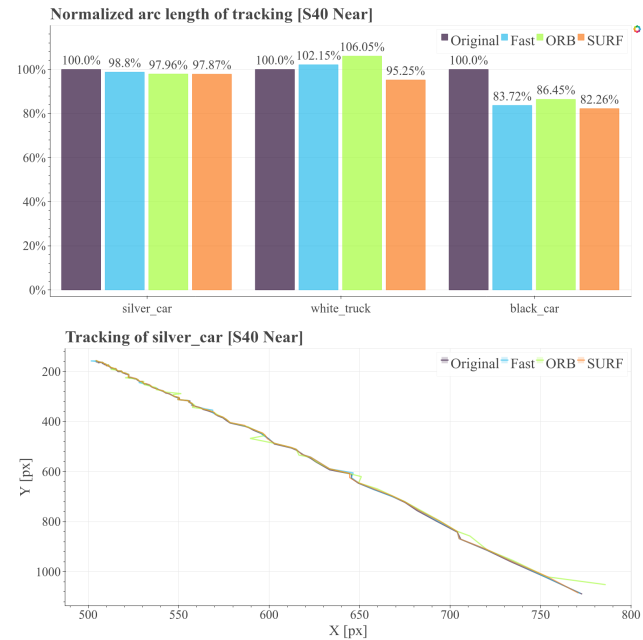
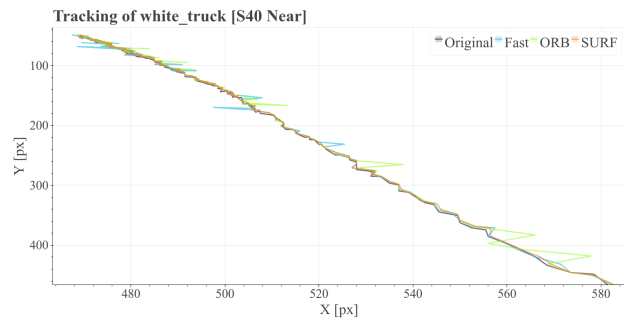
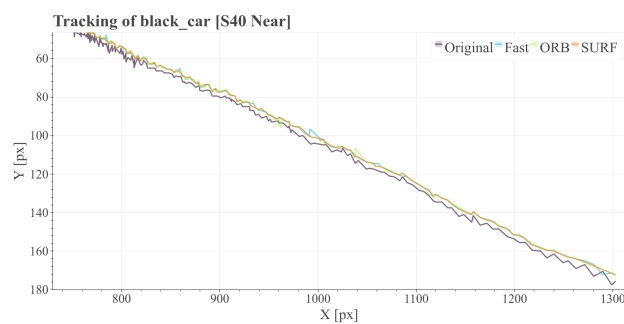


Figure 14. Top left: The tracked vehicles in the camera S40 Near marked by their bounding boxes. Top right: The normalized arc lengths representing the path of the tracked pixels through the image. Bottom graphs: The tracked pixel locations of the vehicles as they move through the scene for the original video feed and the stabilized ones. It shows that the recording did not include much jitter and thus the paths are already relatively smooth, but smoothed further after stabilization.

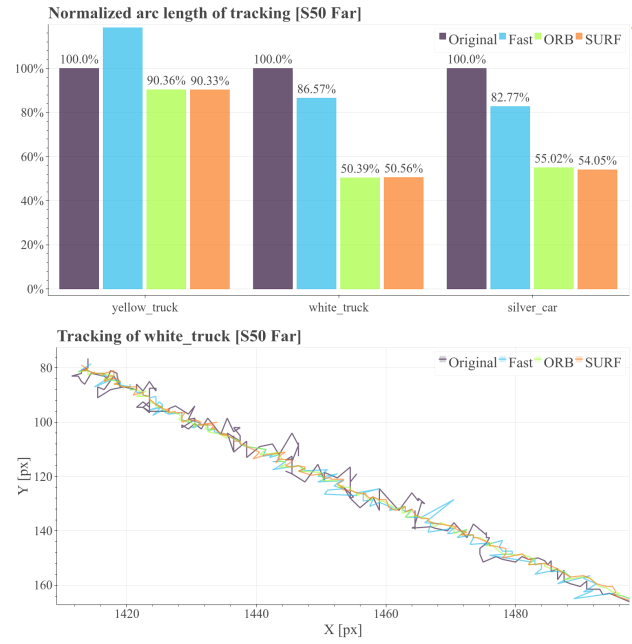
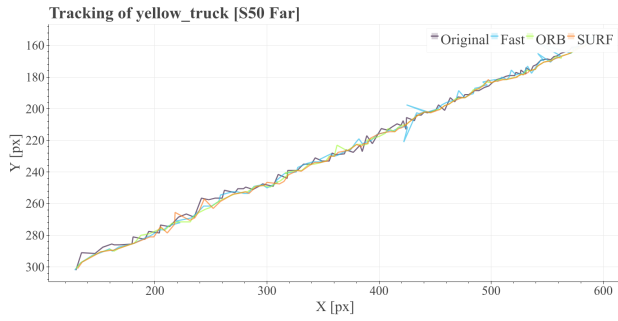
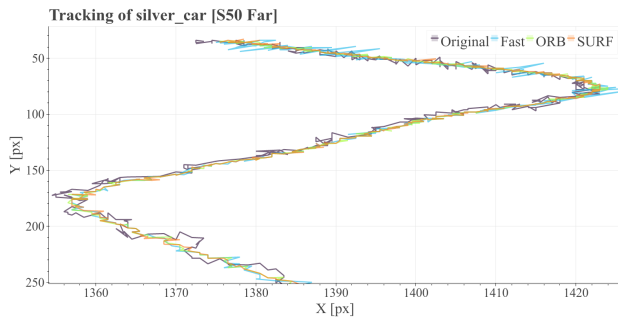
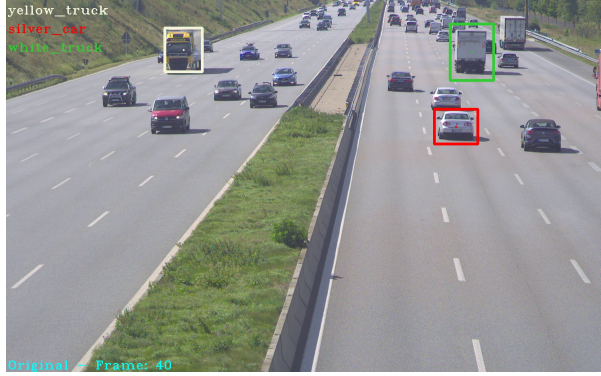


Figure 15. Top left: The tracked vehicles in the camera S50 Far marked by their bounding boxes. Top right: The normalized arc lengths representing the path of the tracked pixels through the image. Bottom graphs: The tracked pixel locations of the vehicles as they move through the scene for the original video feed and the stabilized ones. The jittery motion of the camera can be clearly seen by the chaotic movement of the pixels in the original sequence. After stabilization the pixels move much more smoothly through the images, whereas the remaining jitter is mostly due to inaccuracies in the tracking. The tracking of the silver car displays a lane change of the vehicle over two lanes. The tracking of the yellow truck displays an outlier for FAST as it extended the path of the tracked pixel.



Figure 16. Top left: The tracked vehicles in the camera S50 Near marked by their bounding boxes. Top right: The normalized arc lengths representing the path of the tracked pixels through the image. Bottom graphs: The tracked pixel locations of the vehicles as they move through the scene for the original video feed and the stabilized ones. It shows that the recording did not include much jitter and thus the paths are already relatively smooth, but smoothed further after stabilization.

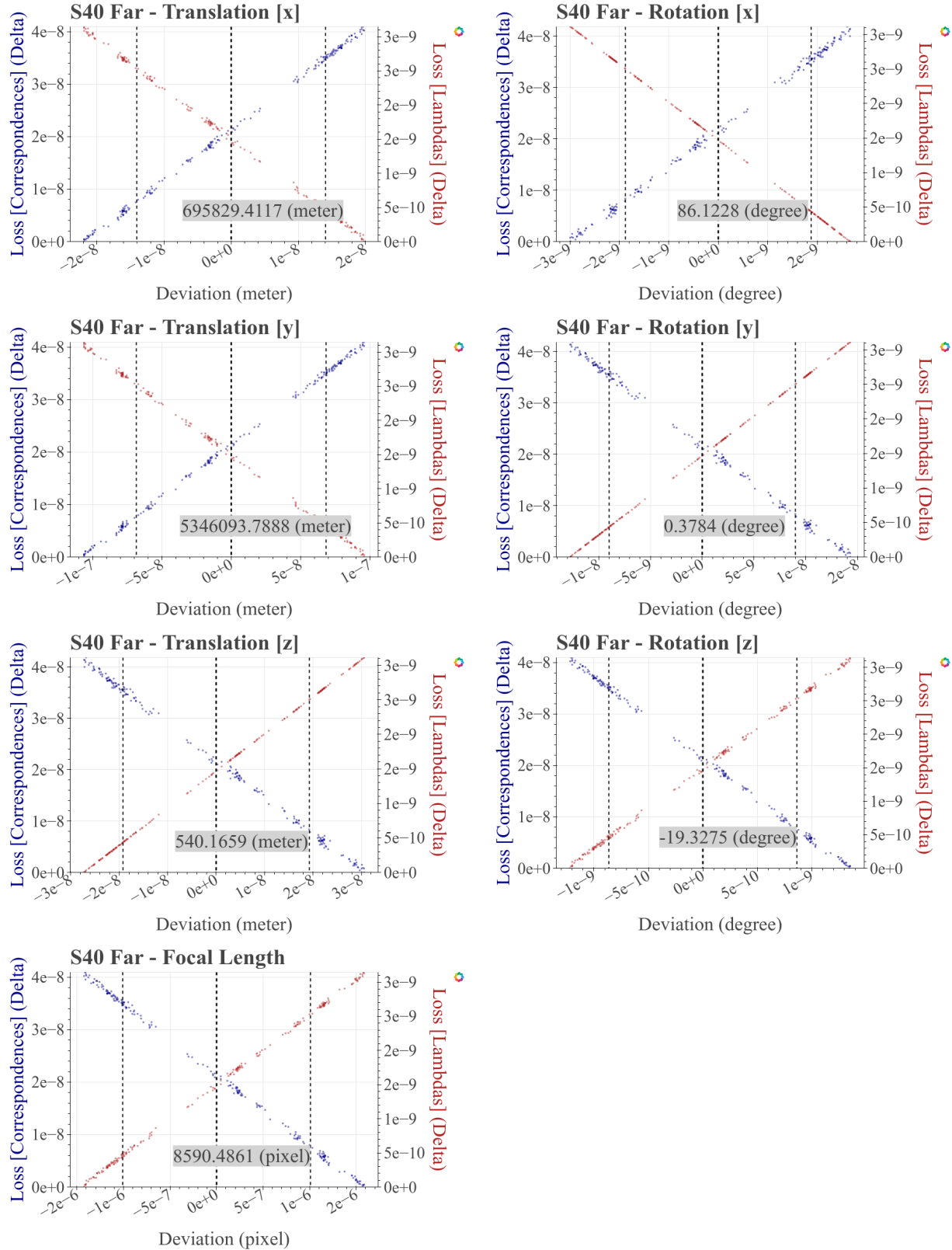


Figure 17. Camera: S40 Far. Left: The resulting translational parameters plotted against the remaining losses. Right: The resulting rotational parameters plotted against the remaining losses. Bottom: The resulting focal length plotted against the remaining losses. For visualization only the relative remaining losses are plotted, as the absolute values have no valuable meaning.

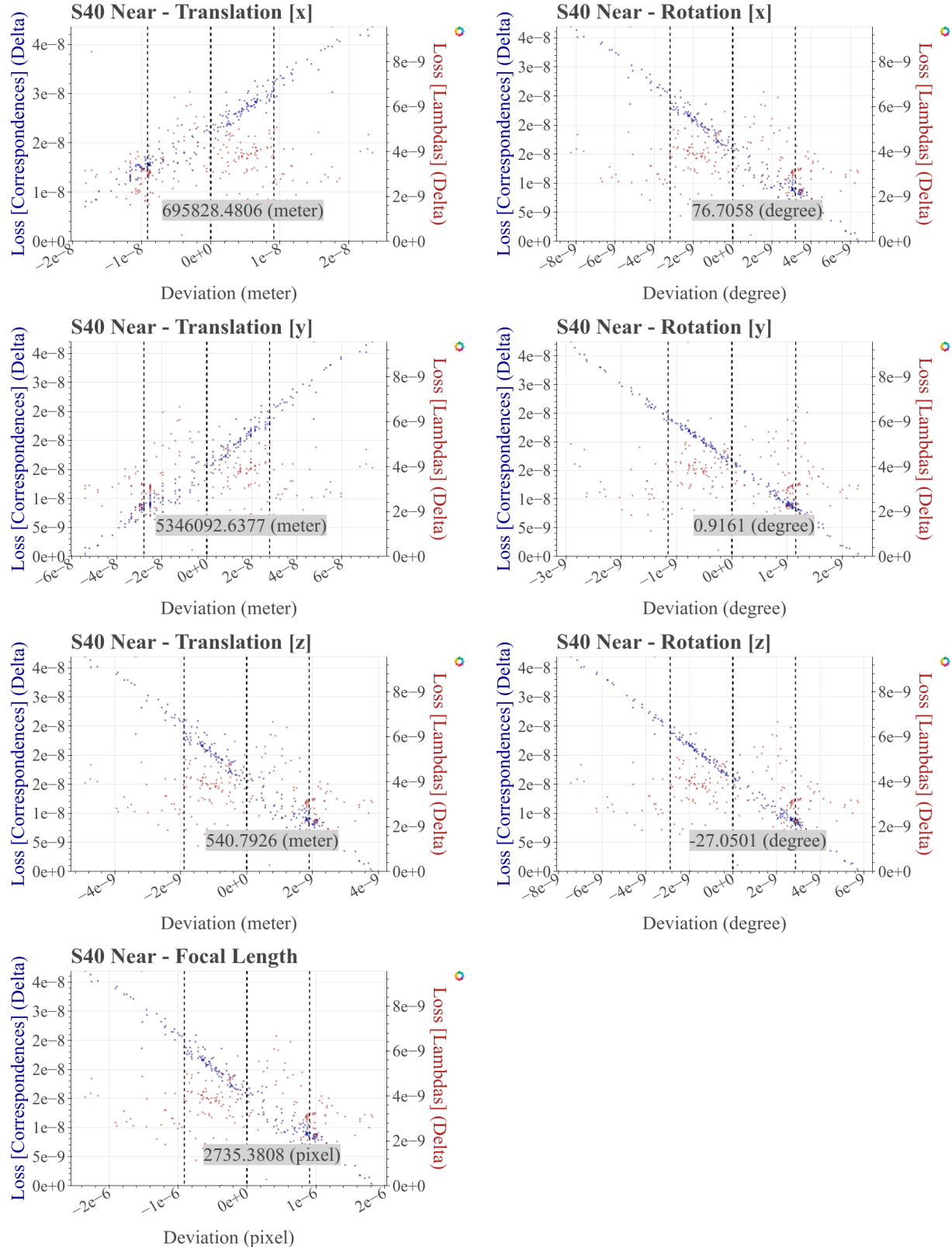


Figure 18. Camera: S40 Near. Left: The resulting translational parameters plotted against the remaining losses. Right: The resulting rotational parameters plotted against the remaining losses. Bottom: The resulting focal length plotted against the remaining losses. For visualization only the relative remaining losses are plotted, as the absolute values have no valuable meaning.

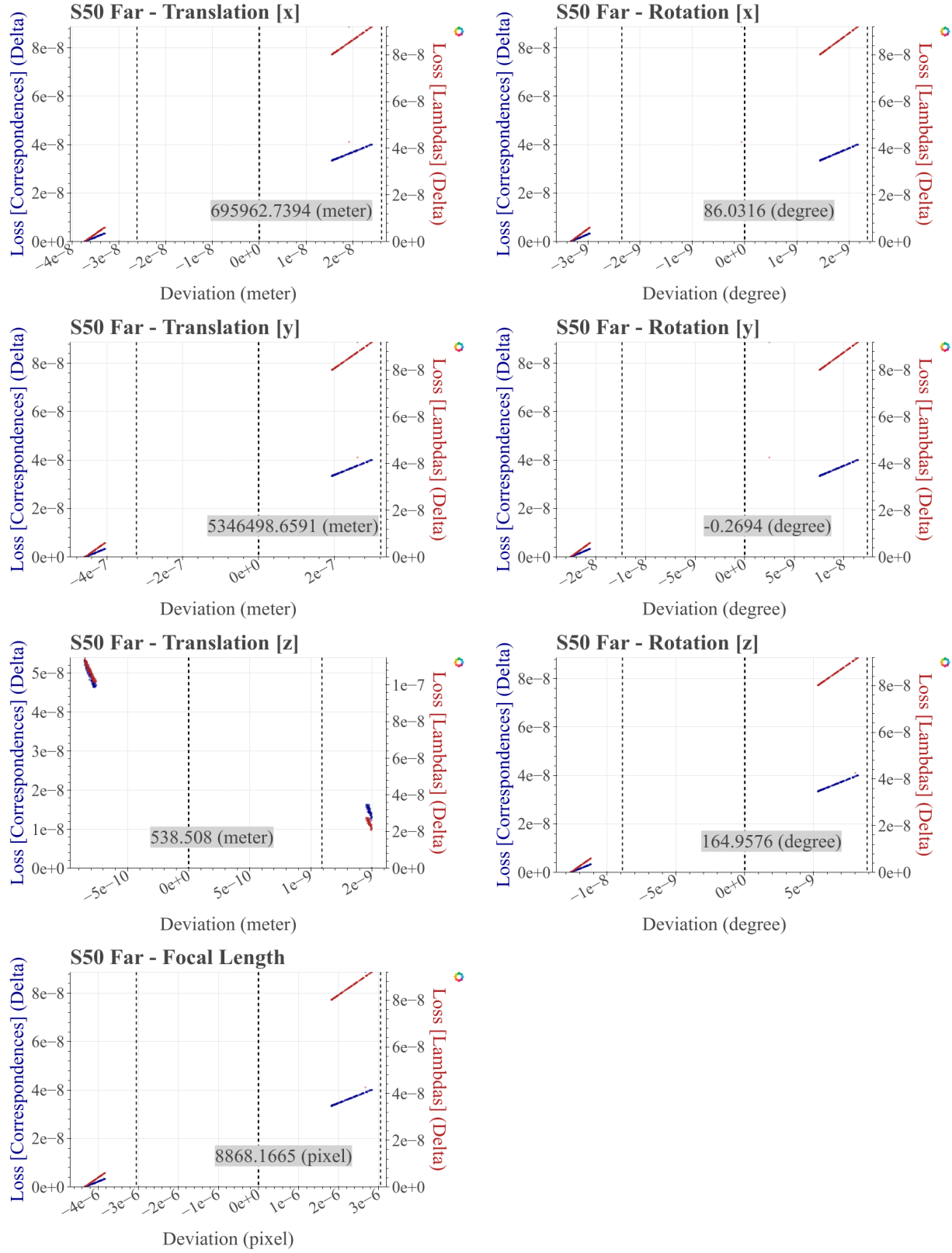


Figure 19. Camera: S50 Far. Left: The resulting translational parameters plotted against the remaining losses. Right: The resulting rotational parameters plotted against the remaining losses. Bottom: The resulting focal length plotted against the remaining losses. For visualization only the relative remaining losses are plotted, as the absolute values have no valuable meaning.

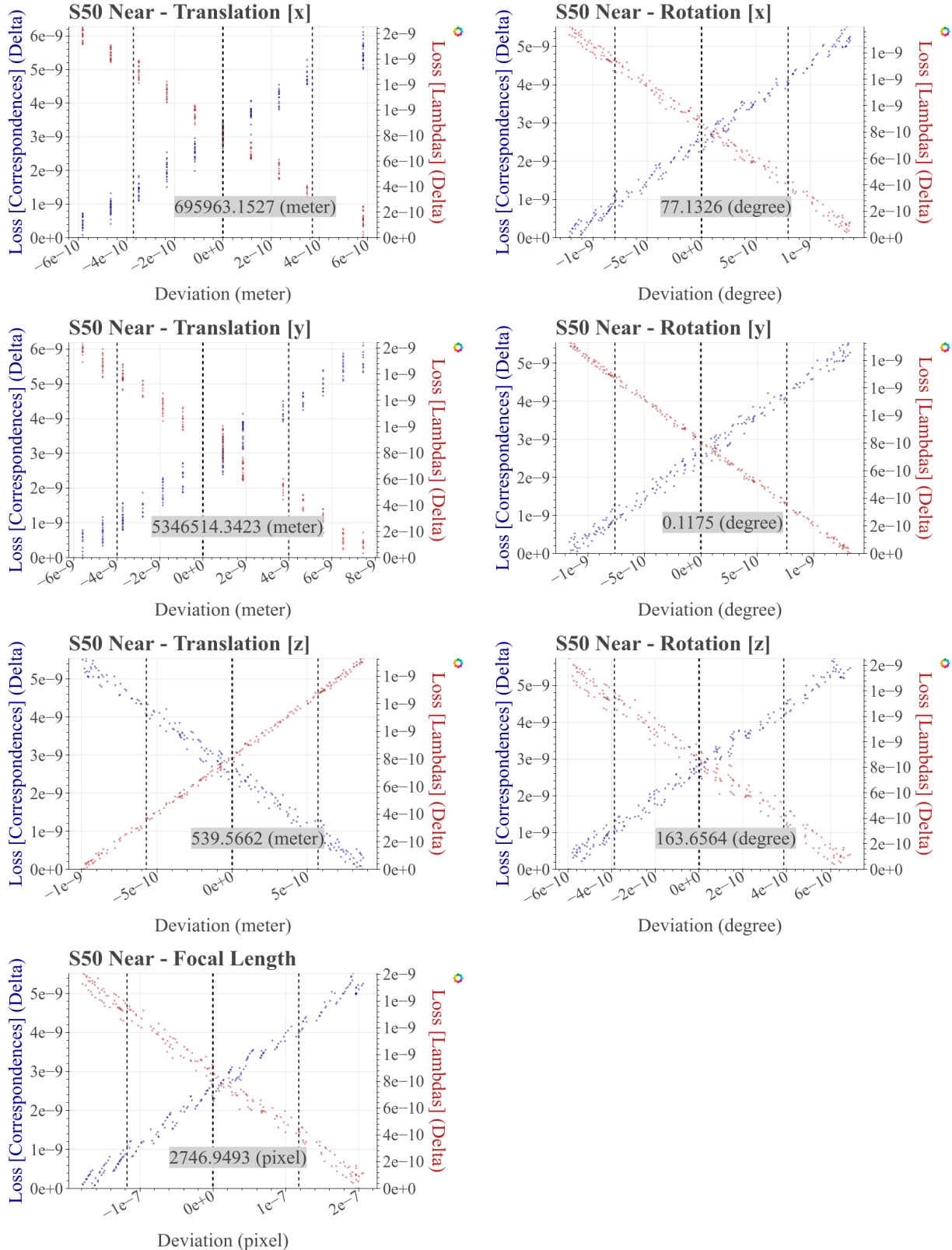


Figure 20. Camera: S50 Near. Left: The resulting translational parameters plotted against the remaining losses. Right: The resulting rotational parameters plotted against the remaining losses. Bottom: The resulting focal length plotted against the remaining losses. For visualization only the relative remaining losses are plotted, as the absolute values have no valuable meaning.